

The Influence of Antenna Pattern on Faraday Rotation in Remote Sensing at L-Band

David M. Le Vine, *Fellow, IEEE*, S. Daniel Jacob, Emmanuel P. Dinnat, Paolo de Matthaëis, *Member, IEEE*, and Saji Abraham, *Senior Member, IEEE*

Abstract—The influence of the pattern of the receive antenna on measured Faraday rotation is examined in the context of passive remote sensing of soil moisture and ocean salinity at L-band. Faraday rotation is an important consideration for radiometers on future missions in space, such as SMOS and Aquarius. Using the radiometer on Aquarius as an example, it is shown that, while $I = T_v + T_h$ is independent of Faraday rotation to first order, it has rotation dependence when realistic antenna patterns are included in the analysis. In addition, it is shown that using the third Stokes parameter to measure the rotation angle can yield a result that is biased by as much as 1° by purely geometrical issues that are associated with the finite width of the main beam.

Index Terms—Antenna patterns, Faraday rotation, microwave remote sensing, radiometer.

I. INTRODUCTION

FARADAY rotation is a change in the polarization vector that occurs as electromagnetic waves propagate through the ionosphere. The magnitude of the change varies as $1/(\text{frequency})^2$ and is an important consideration for remote sensing at the low-frequency end of the microwave spectrum. For example, at L-band (1.4 GHz), where remote sensing of soil moisture and sea surface salinity is performed, the rotation of the polarization vector can range from a few degrees to more than 15° , depending on viewing angle and the solar cycle [1]. The corresponding change in apparent brightness temperature can be several kelvin and is an important issue for missions such as SMOS (Soil Moisture and Ocean Salinity) [2], [3] and Aquarius [4], [5] which will be launched soon to measure soil moisture and sea surface salinity at L-band.

Unfortunately, current models for the ionosphere are often not sufficiently accurate to make corrections [6]. This is particularly true in the case of sea surface salinity, which requires high accuracy and measurements over the oceans [4], [7] where data on the ionosphere is sparse.

Among the strategies that are adopted to avoid the changes due to Faraday rotation is to use the first Stokes parameter

$I = T_v + T_h$. In the ideal case when the antenna patterns for the two polarizations are identical and there is no cross-polarization coupling, I is independent of Faraday rotation. It is also independent of other rotations such as errors in the antenna polarization clocking angle (mechanical misalignment in the plane perpendicular to antenna boresight that causes the axes corresponding to H- and V-polarization to be rotated relative to their desired position).

Another strategy is to measure the third Stokes parameter TU [see (5) for a definition]. One can show that the ratio of TU to the second Stokes parameter $Q = T_v - T_h$ is proportional to the tangent of twice the angle of Faraday rotation. This was recognized by Yueh, who described how TU and Q could be used to measure the Faraday rotation [8]. The use of TU to measure Faraday rotation has been described in the context of SMOS [9], and an analysis of the impact of Faraday rotation on the measurement of TU by Windsat has been described [10].

Both of these strategies work in the case of narrow beam antennas with no cross-polarization coupling. However, at L-band, antennas in space tend to have large footprints (e.g., 100-km diameter for Aquarius) and small but not negligible cross-polarization coupling. The purpose of this paper is to examine the performance of these two approaches when used with antennas with realistic patterns. Of concern are the effect of cross-polarization coupling, the mismatch of the patterns for the two polarizations, and the effect of changes in the orientation of the polarization vectors at the surface with respect to boresight over the footprint of the antenna beam. For example, cross-polarization coupling can introduce a dependence on Faraday rotation in the sum $I = T_v + T_h$ and also introduce a bias in the estimate of the angle of Faraday rotation that is obtained from Q and TU . In the sections to follow, expressions for I , Q , and TU are derived for a general antenna and examined in special cases. Then, to get realistic estimates of the magnitude of the effects to be expected in the general case, the patterns of the antennas for the Aquarius radiometer are used to generate numerical results.

II. ANTENNA TEMPERATURE: GENERAL CASE

Consider a dual-polarized antenna with its two polarization ports \mathbf{v} and \mathbf{h} arranged, so that at boresight, the directions correspond to the conventional definitions at the surface, i.e.,

$$\begin{aligned}\mathbf{h} &= (\mathbf{k} \times \mathbf{n})/|\mathbf{k} \times \mathbf{n}| \\ \mathbf{v} &= \mathbf{h} \times \mathbf{k}\end{aligned}\quad (1)$$

Manuscript received December 21, 2006; revised February 28, 2007.

D. M. Le Vine is with the Instrument Sciences Branch, Laboratory for Hydrospheric and Biospheric Sciences, Goddard Space Flight Center, Greenbelt, MD 20771 USA.

S. D. Jacob, E. P. Dinnat, and P. de Matthaëis are with the Goddard Earth Science and Technology Center, Goddard Space Flight Center, Greenbelt, MD 20771 USA.

S. Abraham is with RS Information Systems, Inc., Goddard Space Flight Center, Greenbelt, MD 20771 USA.

Color versions of one or more of the figures in this paper are available online at <http://ieeexplore.ieee.org>.

Digital Object Identifier 10.1109/TGRS.2007.898237

where \mathbf{n} is a vector normal to the surface, and \mathbf{k} is the direction of propagation from the surface toward the antenna. Let the antenna “voltage” pattern at each port be

$$\begin{aligned} \mathbf{G}_h &= g_{hh}\boldsymbol{\varepsilon}_2 + g_{hv}\boldsymbol{\varepsilon}_1 \\ \mathbf{G}_v &= g_{vv}\boldsymbol{\varepsilon}_1 + g_{vh}\boldsymbol{\varepsilon}_2 \end{aligned} \quad (2)$$

where g_{ij} are complex, and $\boldsymbol{\varepsilon}_i$ are unit vectors defined by Ludwig [11] to indicate the directions of copolarization and cross polarization. Assume a local coordinate system at the antenna with unit vectors $(\mathbf{x}, \mathbf{y}, \mathbf{z})$, and let the z -axis be along the boresight direction (pointing to the surface) and let the x -axis be aligned with the direction of vertical polarization \mathbf{v} at the surface. Then, one has [11]

$$\begin{aligned} \boldsymbol{\varepsilon}_1 &= [1 + \cos^2 \varphi (\cos \theta - 1)] \mathbf{x} \\ &\quad + (\cos \theta - 1) \sin \varphi \cos \varphi \mathbf{y} - \sin \theta \cos \varphi \mathbf{z} \\ \boldsymbol{\varepsilon}_2 &= (\cos \theta - 1) \sin \varphi \cos \varphi \mathbf{x} \\ &\quad + [1 + \sin^2 \varphi (\cos \theta - 1)] \mathbf{y} - \sin \theta \sin \varphi \mathbf{z}. \end{aligned} \quad (3)$$

The antenna output, i.e., antenna temperature T_A , can be written in the form [12]

$$T_A = \int G(\Omega)R(\Omega)T_B(\Omega) d\Omega \quad (4)$$

where T_B is the “modified” Stokes vector, in units of brightness temperature, evaluated at the surface

$$T_B = \begin{bmatrix} T_v \\ T_h \\ T_3 \\ T_4 \end{bmatrix} \quad (5)$$

where $T_3 = T_U = 2\alpha \text{Re}\langle E_h^* E_v \rangle$, and $T_4 = T_V = 2\alpha \text{Im}\langle E_h^* E_v \rangle$. In these expressions, E_v and E_h are the electric fields of vertical and horizontal polarizations, respectively; the coefficient of proportionality is $\alpha = \lambda^2 / (\eta k)$, where $\eta = \sqrt{\mu/\varepsilon}$ is the intrinsic impedance of the medium, k is Boltzmann’s constant, and $\langle \rangle$ indicates the expected value.

In (4), R is a “rotation” matrix given by

$$R = \begin{bmatrix} \cos^2 \varphi_c & \sin^2 \varphi_c & 0.5 \sin 2\varphi_c & 0 \\ \sin^2 \varphi_c & \cos^2 \varphi_c & -0.5 \sin 2\varphi_c & 0 \\ \sin 2\varphi_c & -\sin 2\varphi_c & -\cos 2\varphi_c & 0 \\ 0 & 0 & 0 & -1 \end{bmatrix} \quad (6)$$

and G in (4) is an antenna pattern matrix given by (7), shown at the bottom of the page.

The matrix in (7) appears in scattering theory where the parameters g_{ij} are replaced by scattering coefficients, and it is commonly called the “Stokes matrix” [13], [14].

In (6), the angle $\varphi_c = \varphi + \Phi_F$, where Φ_F is the Faraday rotation angle (Appendix B-I) and φ is a geometry-dependent rotation. The latter occurs because the polarization vectors that are defined on the surface [\mathbf{h} and \mathbf{v} in (1)] are aligned with the polarization vectors of the antenna (3) only at boresight. Along other rays from the surface to the antenna, the polarization vectors at the surface are rotated relative to the vectors that were defined in (3) (see Appendix B-II and also [15]). Although not considered here, it is also possible to have a rotation about boresight of the antenna polarization vectors themselves relative to the desired orientation (e.g., a misalignment of the polarization vectors due to mechanical error). This would appear as a constant offset φ_0 that would be included in φ_c .

III. SPECIAL CASES

The matrix operations that result from substituting (5)–(7) into the integrand of (4) are straightforward, but the expressions that result are rather long. The general expressions are given in Appendix A, and they will be used for the numerical computations to be discussed in the following (Section IV). However, in order to gain insight, it is convenient to first look at special cases. In the following discussion, $I = T_v + T_h$, $Q = T_v - T_h$, and $T_3 = 2\alpha \text{Re}\langle E_h^* E_v \rangle$. Parameters without primes are measured at the surface. Parameters with primes (i.e., I' , Q' , and T_3') have the same definition but are measured at the sensor after propagation through the ionosphere and after being weighted by the antenna pattern (7) but before integration. That is, they are the result of the matrix product $G(\Omega)R(\Omega)T_B(\Omega)$ in (4).

A. Ideal Antenna Patterns

The general expressions simplify greatly if one assumes that the antenna patterns for the two polarizations are identical and that there is no cross-polarization coupling. In particular, assume $g_{hh} = g_{vv} = G$, and $g_{hv} = g_{vh} = 0$. In this case, one obtains the conventional results, and the first Stokes parameter $I' = T_v' + T_h'$ is independent of Faraday rotation. Combining the first two rows in the integrand in (4), one obtains

$$I' = G^2 I \quad (8a)$$

$$Q' = G^2 \cos(2\varphi_c) Q + G^2 \sin(2\varphi_c) T_3 \quad (8b)$$

$$T_3' = G^2 \sin(2\varphi_c) Q - G^2 \cos(2\varphi_c) T_3 \quad (8c)$$

where it has been assumed that $T_4 = 0$ at the surface, but $T_3 \neq 0$ and the primes on the quantities on the left are a reminder that the integration in (4) has not been done.

$$G = \begin{bmatrix} |g_{vv}|^2 & |g_{vh}|^2 & \text{Re}(g_{vv}g_{vh}^*) & -\text{Im}(g_{vv}g_{vh}^*) \\ |g_{hv}|^2 & |g_{hh}|^2 & \text{Re}(g_{hh}g_{hv}^*) & -\text{Im}(g_{hh}g_{hv}^*) \\ 2\text{Re}(g_{vv}g_{hh}^*) & 2\text{Re}(g_{hh}g_{vh}^*) & \text{Re}(g_{vv}g_{hh}^* + g_{vh}g_{hv}^*) & -\text{Im}(g_{vv}g_{hh}^* - g_{vh}g_{hv}^*) \\ 2\text{Im}(g_{vv}g_{hh}^*) & 2\text{Im}(g_{hh}g_{vh}^*) & \text{Im}(g_{vv}g_{hh}^* + g_{vh}g_{hv}^*) & \text{Re}(g_{vv}g_{hh}^* - g_{vh}g_{hv}^*) \end{bmatrix} \quad (7)$$

Notice that, in this case, I' is independent, not only of Faraday rotation Φ_F but also of any geometrical effects φ . As mentioned previously, a nonzero value of φ can arise because the polarization vectors at the surface are not aligned with the polarization vectors as defined at the antenna ports (Appendix B-I). In the ideal case, the first Stokes parameter has the added advantage of being independent of both φ and Φ_F .

In addition, notice that, when the third Stokes parameter at the surface T3 is zero, then the ratio $T3'/Q'$ is proportional to the tangent of $2\varphi_c$

$$\varphi_c = 0.5 \tan^{-1}(T3'/Q'). \quad (9)$$

Yueh [8] proposed the use of $T3'$ and Q' in this manner to measure Faraday rotation. He discussed the impact on the retrieval when the third Stokes parameter at the surface T3 is not zero. However, he did not consider the effects of the integration over the footprint (i.e., the integration in (4) remains to be performed). For a very narrow antenna pattern, this is not an issue. However, for a broad antenna pattern such as is likely to be the case at L-band for antennas in space [4], the variation of geometry over the footprint must be taken into account. As will be shown in the examples later, a bias can arise due to nonzero φ when this integration is performed.

B. Impact of Cross-Polarization Coupling

Let the antenna patterns be identical as in the preceding case, but in this case, assume nonzero cross-polarization coupling. That is, assume $g_{hh} = g_{vv} = G$ as before, but instead of zero cross-polarization coupling, assume $g_{hv} = g_{vh} = g$. In this case, the terms in the integrand in (4) can be written in the form

$$\begin{aligned} I' &= (G^2 + g^2)I + 2\text{Re}(Gg^*) \sin(2\varphi_c)Q \\ &\quad - 2\text{Re}(Gg^*) \cos(2\varphi_c)T3 \\ Q' &= (G^2 - g^2) \cos(2\varphi_c)Q + (G^2 - g^2) \sin(2\varphi_c)T3 \\ T3' &= -(G^2 + g^2) \cos(2\varphi_c)T3 + 2\text{Re}(Gg^*)I \\ &\quad + (G^2 + g^2) \sin(2\varphi_c)Q. \end{aligned} \quad (10)$$

In most cases, g is small, and $g^2 \ll G^2$. Assuming this to be the case and keeping only terms of first order in g , the results simplify to

$$I' = G^2 I + 2\text{Re}(Gg^*) \sin(2\varphi_c)Q - 2\text{Re}(Gg^*) \cos(2\varphi_c)T3 \quad (11a)$$

$$Q' = G^2 \cos(2\varphi_c)Q + G^2 \sin(2\varphi_c)T3 \quad (11b)$$

$$T3' = -G^2 \cos(2\varphi_c)T3 + 2\text{Re}(Gg^*)I + G^2 \sin(2\varphi_c)Q. \quad (11c)$$

Even neglecting T3, which is likely to be very small at L-band [8], the first Stokes parameter I' is now no longer independent of either Faraday rotation or geometry effects φ . In addition, now it is coupled to the second Stokes parameter Q

and, therefore, is likely to be more dependent on local incidence angle θ than before. At modest incident angles and flat surfaces with no roughness, $I = Tv + Th$ is almost constant, but $Q = Tv - Th$ increases with incidence angle. In addition, even when $T3 = 0$, the third Stokes parameter at the sensor $T3'$ now is biased relative to its value in the ideal case by the factor $2\text{Re}(Gg^*)I$. This term is independent of φ_c . Assuming $g \ll G$ and $\cos(2\varphi_c) \approx 1$, one can apply (9) to retrieve Faraday rotation, but now the result will be biased by a term that depends on the magnitude of (gI/GQ) .

C. Size of the Footprint

The preceding discussion does not include the effects of the integration in (4) over the antenna pattern. It does apply to an antenna with a narrow beam because, in this case, to a first approximation, the integrand can be pulled out of the integral. However, with the relatively broad main beams likely at L-band, variations over the footprint must be taken into account [15]. Even in the idealized case (8), I and Q obtained from the apparent antenna temperature T_A on the left-hand side of (4) can differ from their values at boresight because of variations of the local incidence angle over the footprint. The same is true in the situation described in (11), although more complex because, in addition to changes in I and Q with incidence angle, φ_c can vary over the footprint. To get an idea of the magnitude of these effects, numerical examples are presented in the following section.

IV. EXAMPLE

In order to obtain a more complete picture of how important the size of the antenna footprint and the presence of cross-polarization coupling are in a realistic case, the integration in (4) has been evaluated using the antenna patterns for the radiometer being developed for the Aquarius instrument [4], [5]. Aquarius is an L-band microwave instrument being developed to map the salinity field at the surface of the ocean from space. It is part of the Aquarius/SAC-D mission, which is a partnership between the U.S. (NASA) and Argentina (CONAE) [16]. The Aquarius antenna is a 2.5-m offset parabolic reflector with three feed horns. The three beams are arranged to image in pushbroom fashion, with the beams pointed across track, which is roughly 90° with respect to the spacecraft heading, at look angles of 25.8° , 33.8° , and 40.3° with respect to the satellite nadir. The resolution of the three radiometer beams ranges from 76×94 km for the inner beam to 97×157 km for the outer beam, and the antennas have a beam width (full width at half maximum) of about 6.5° . The antenna patterns (copolarization and cross polarization) for the horizontally polarized port of the outer beam are shown in Fig. 1. The patterns for the other beams are similar (e.g., [15, Fig. 2]). These are calculated antenna patterns that were developed with modern antenna modeling tools and provided by the Aquarius antenna engineering team, and have recently been validated with measurements on a scale model [17].

Calculations have been made using the antenna patterns that were described previously and the orbit geometry of the

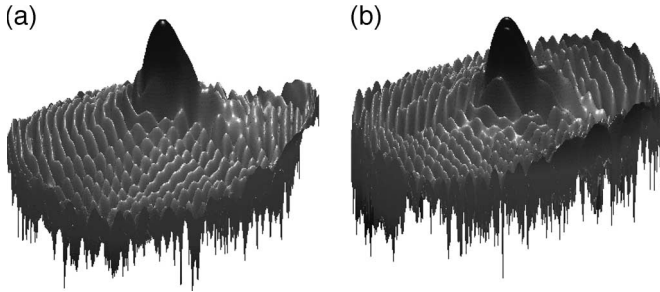


Fig. 1. Example antenna patterns. Shown are (a) the co-polarized pattern and (b) the cross-polarized pattern for the horizontally polarized channel of the outermost beam in the Aquarius radiometer. The peak level in (a) is about 25 dB more than that in (b).

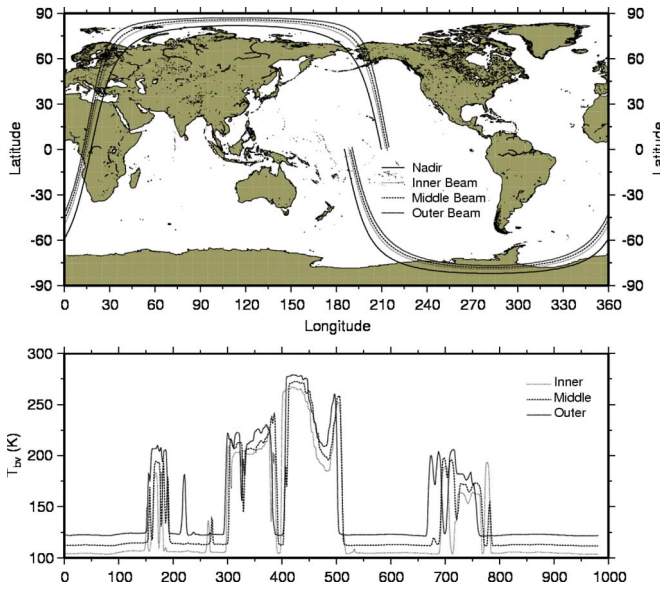


Fig. 2. (Top) Ground track (bold) and beam boresight for each of the three Aquarius radiometer beams during one orbit. (Bottom) Brightness temperature at vertical polarization for the three beams during this orbit. The large jumps in level occur at the transitions from land to water. The different values over water reflect the different incidence angles of the three beams. The index on the horizontal axis at the bottom panel indicates sample points in the calculations (one calculation every 6 s).

Aquarius sensor. Aquarius will be launched into a sun-synchronous orbit at an altitude of 657 km, an inclination of 98°, and equatorial crossing times of 6 A.M. (descending) and 6 P.M. (ascending). The orbit is a seven-day exact repeat orbit. Fig. 2 (top) shows the ground track for a representative orbit (bold solid line) and the intersection of the boresight ray with the surface for the three beams (dotted lines). The Aquarius antenna patterns are used for the elements of matrix G in (7), and the orbit geometry that is shown in Fig. 2 is used to evaluate the elements of matrix R in (6) and also to determine the brightness temperature vector at the surface T_B . An example of antenna temperature T_v , which is obtained in this manner from (4), is shown in Fig. 2 (bottom). Values are shown for each of the three beams during one orbit. The horizontal axis (abscissa) is labeled in sample points around the orbit. The calculations are done once every 6 s, and the results are numbered (1–980) and plotted sequentially as the spacecraft orbits. The large

changes in antenna temperature occur at water/land boundaries and are due to a large difference in emissivity of land compared to water. The jumps are slightly displaced relative to each other because the beam centers are not coaligned [see the dotted lines in Fig. 2 (top)].

In order to keep the focus on the issue of Faraday rotation, a number of simplifications have been made in the calculations. First, it will be assumed that the off-earth contributions such as the sun and cosmic background are zero, in which case only the integration over the visible disk is relevant (see [15] for a discussion of the effect of the integration over the off-earth background). Second, it is assumed that the surface consists of only water at a constant temperature (25 °C) and a constant salinity (35 psu). This eliminates the jumps and small variations that are seen in Fig. 2 (bottom) due to land/water crossings and naturally occurring changes in water parameters, which otherwise would distract from the issues at hand. Finally, all factors other than Faraday rotation, which normally contribute to the observed antenna temperature (e.g., atmospheric emission and attenuation, reflected radiation from the sun, and cosmic background) have been set to zero. With these assumptions, the only contribution other than radiation from the surface is due to Faraday rotation. Faraday rotation is computed using the IRI-2000 to model the ionosphere [18] and the International Geomagnetic Reference Field (IGRF) for the Earth magnetic field [19]. Details are given in Appendix B.

A. Ideal Case

In the ideal case, the antenna patterns at each polarization are identical, and there is no cross-polarization coupling. The integrand in this case is given in (8), and the integration in (4) will be done numerically using the pattern for the H-polarization channel of Aquarius radiometer that is shown in Fig. 1. The co-polarized pattern is used for both the H- and V-polarized channels and the cross-polarization coupling terms [g_{vh} and g_{hv} in (2)] are set to zero. The pattern was renormalized to account for the fact that the integration is only over the visible disk [15].

1) *First Stokes Parameter:* As expected from (8a), the first Stokes parameter $I = T_v + T_h$ is essentially constant around the orbit and independent of Faraday rotation. However, the value that was obtained after integration is not exactly the same as the value at boresight. This is shown in Table I, which gives the values that were obtained for the three beams at boresight and after integration. The integrated value differs from its value at boresight because the local incidence angle ranges from 0° to about 65° over the visible disk, and there is enough energy in the antenna pattern at large incidence angles to make a small difference.

2) *Retrieved Rotation Angle:* Figs. 3 and 4 show the angle that was retrieved using the ratio of the second and third Stokes parameters. In this case, the integration in (4) is done as described previously, and the rotation angle is obtained from

$$\varphi_c = 0.5 \tan^{-1}(T3_A/Q_A) \tag{12}$$

where subscript “A” is a reminder that these are the values, after integration, obtained from the antenna temperature vector

TABLE I
FIRST STOKES PARAMETER

Beam	I = Tv + Th	
	Integrated	Boresight
Inner Beam	182.6	182.4
Middle Beam	184.7	184.3
Outer Beam	188.7	187.7

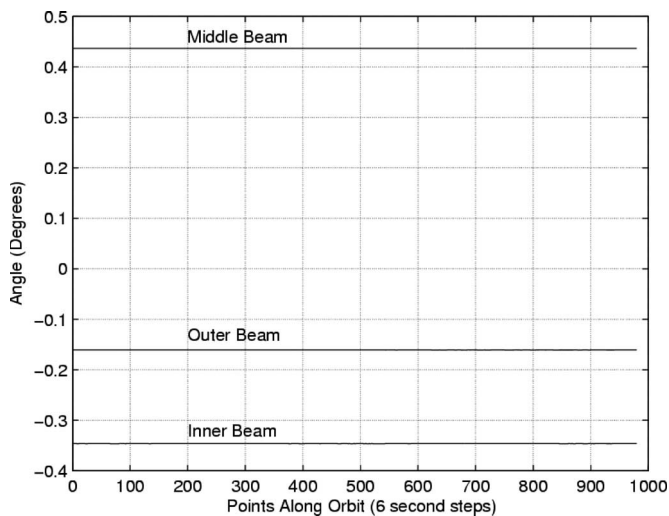


Fig. 3. Retrieved angle in the ideal case (identical patterns with no cross polarization) and no Faraday rotation. The angle is due to changes in geometry over the antenna footprint.

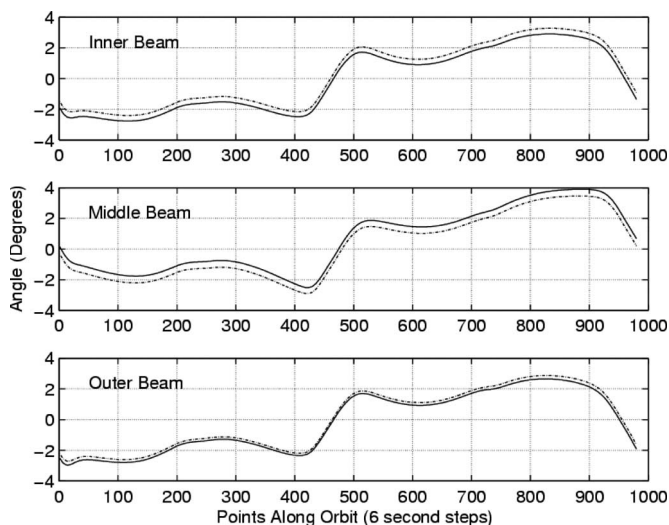


Fig. 4. Retrieved angle during one orbit in the ideal case with Faraday rotation included. The dominant contribution is due to Faraday rotation. The dashed line is the value at boresight. The sign changes occur at equatorial crossings (0 and 450) due to the change in the sign of the magnetic field “dip” angle.

T_A. Fig. 3 shows the retrieved angle in the case of no Faraday rotation to illustrate the impact of purely geometrical factors. The vertical axis is the retrieved angle, and the horizontal axis is labeled in sample points along the orbit: The spacecraft starts on the equator (index “1”), and 6 s later, a second calculation is made (index “2”), continuing in 6-s steps until the spacecraft rotates one orbit (index “980”). The three curves show the

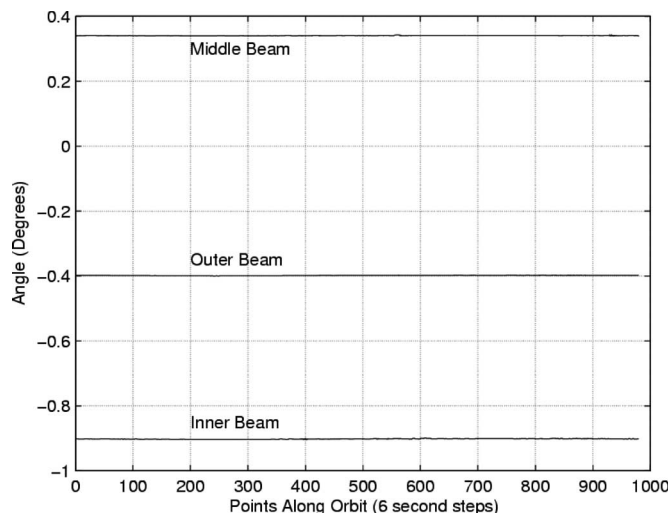


Fig. 5. Effect of cross-polarization coupling on the retrieved angle. This is the same as the case in Fig. 3, with idealized pattern and no Faraday rotation, but with cross-polarization coupling included.

retrieved angle for the three Aquarius beams. Since the Faraday rotation is zero, the retrieved angle is due to variations of the polarization vectors at the surface over the field of view of the antenna relative to their values at boresight. The angle is constant because the geometry changes very little as the spacecraft orbits (there is a small change in altitude). The retrieved angle is different for the three beams because the antenna patterns and boresight direction are different.

Fig. 4 shows the angles that were retrieved using (12) but with Faraday rotation included. In this case, the dominant contribution to φ_c is no longer geometry but Faraday rotation in the ionosphere. The shape of the curve reflects changes in the electron density and magnetic field along the orbit. The ionosphere is the IRI-2000 model for November 14, 2004, which is a period of low solar activity (LSA). Notice the sign change that occurs when the spacecraft crosses the equator (near index 450). This is due to the change in the “dip” angle of the magnetic field relative to the boresight vector (e.g., [1]). The dashed line gives the Faraday rotation at boresight as a reference, and the solid line is the angle that was retrieved from (12). The slight difference is primarily due to the geometry effects shown in Fig. 3, which are zero at boresight. Faraday rotation depends on the total electron content along the line of sight and the orientation of the line of sight with respect to the local magnetic field. In the case of the three Aquarius beams, the middle beam points slightly aft of across track, and the inner and outer beams point slightly forward. This difference in azimuth accounts for the offset of the middle beam relative to the outer two, which is evident, for example, at the beginning of the record.

B. Effect of Cross-Polarization Coupling

Figs. 5–7 illustrate the impact of cross-polarization coupling (11). The calculations are done as described previously using the pattern for the H-polarized channel for both polarizations, but in this case, with the cross-polarization coupling term included [Fig. 1(b)].

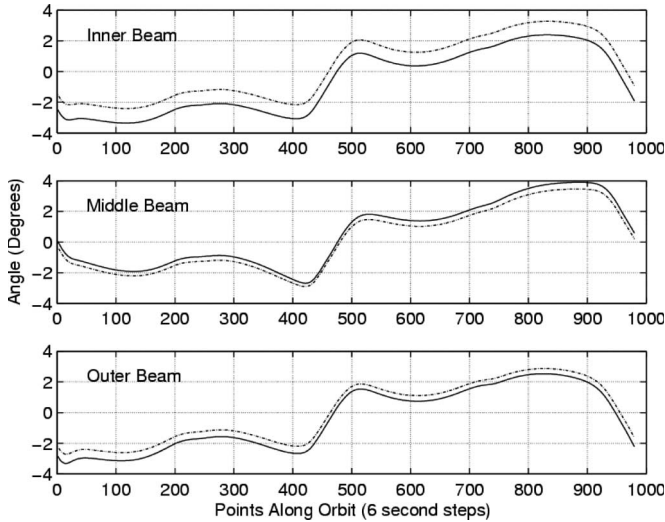


Fig. 6. Effect of cross-polarization coupling on the retrieved Faraday rotation angle. The antenna patterns are the same as in the ideal case but with cross-polarization included. The dotted curve is the value that was retrieved at antenna boresight.

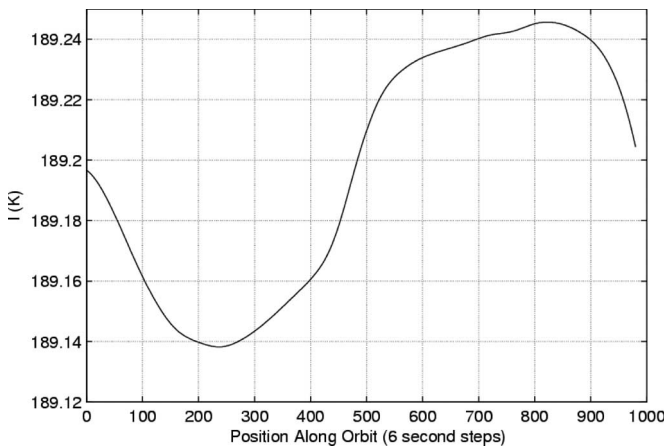


Fig. 7. Effect of cross-polarization coupling on the first Stokes parameter $I = T_v + T_h$ in the special case that was defined by (11). The example that is shown is for the outer beam.

Figs. 5 and 6 show the angle that was retrieved using (12). Fig. 5 shows the case with no Faraday rotation to illustrate the influence of geometric effects on the retrieved angle. Comparing with Fig. 3 indicates that the bias is larger in magnitude for the inner and outer beams and somewhat smaller for the middle beam when cross polarization is included. Fig. 6 shows the case with Faraday rotation. Faraday rotation again dominates the retrieved angle, and as before, the retrieved value is biased relative to the value at boresight. The behavior is similar to that shown in Fig. 4 but with different bias.

Table II shows a comparison of the bias in the cases with cross-polarization coupling (CP) and without cross-polarization coupling (NCP). In the columns labeled “No Faraday Rotation,” these are the values from Figs. 3 and 5. The entries in the columns labeled “Faraday Rotation” are the mean difference between the retrieved angle and the angle at boresight (difference between the dashed and solid curves in Figs. 4

TABLE II
BIAS WITH CROSS-POLARIZATION COUPLING INCLUDED

Beam	No Faraday Rotation		Faraday Rotation*	
	NCP	CP	NCP	CP
Inner	-0.346	-0.903	-0.358	-0.910
Middle	0.436	0.340	0.423	0.332
Outer	-0.161	-0.399	-0.188	-0.426

*Mean difference between value at boresight and retrieved value

and 6). In the case of the inner and outer beams, the magnitude of geometry-induced bias has increased when cross-polarization coupling is included. However, it is slightly smaller for the middle beam. Apparently, this is an indication of the dependence of the bias on the antenna pattern and orientation. Comparing the two columns under “No Faraday Rotation” with their counterparts under “Faraday Rotation,” it is clear that the bias relative to the value at boresight is very close to the geometry-induced bias in both cases with and without cross-polarization coupling. The numbers that are shown in the table are averaged over the orbit, but there was very little variation and the rms value was about the same as the mean value.

Fig. 7 illustrates the impact of cross-polarization coupling on the first Stokes parameter $I = T_v + T_h$. It is clear from (11a) that when cross-polarization coupling is included, the first Stokes parameter is no longer independent of Faraday rotation. This is illustrated in Fig. 7, which shows I for the outer beam obtained by doing the integration in (4) and then adding T_v and T_h . The integration is done as described previously with cross-polarization coupling included but using the same pattern for both the H-polarization and V-polarization ports. The dependence on Faraday rotation is clearly evident. Notice the similarity of the shape of the curve with those in Figs. 4 and 6, which show the retrieved Faraday rotation angle. The dependence is rather small, with a peak–peak change of about 0.1 K. However, if the goal is to measure sea surface salinity with an accuracy of 0.2 psu, which is the goal of the Aquarius mission [4], this is a significant variation since the sensitivity at L-band is about 0.5 K/psu per polarization.

C. General Case

Examples are shown for the general case in Figs. 8 and 9. In this case, the calculations are done using (A4) with the actual antenna patterns for each polarization and each beam. Cross-polarization coupling is included, and the patterns are not identical for each polarization port of the same beam as they were in all the preceding cases.

1) *First Stokes Parameter:* An example of the first Stokes parameter $I = T_v + T_h$ in the general case is shown in Fig. 8. Examples are shown for the outer beam in the case of LSA and high solar activity (HSA). The case for LSA is the same ionosphere used in the previous examples for November 14, 2004, and in this case, the dependence on Faraday rotation is about the same as in the special case that was discussed previously in Section IV-B. There is a slight difference in amplitude between the LSA case in Figs. 7 and 8, but this is probably a coincidence of the patterns that were used and the slight mismatch between the patterns at the two polarization ports, which occurs in the general case. In the case of HSA,

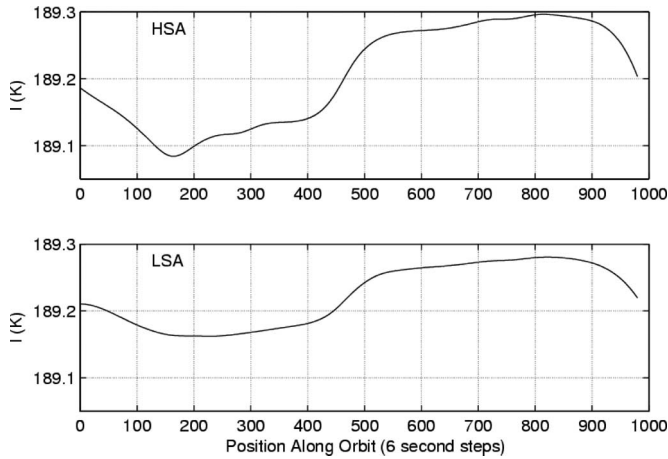
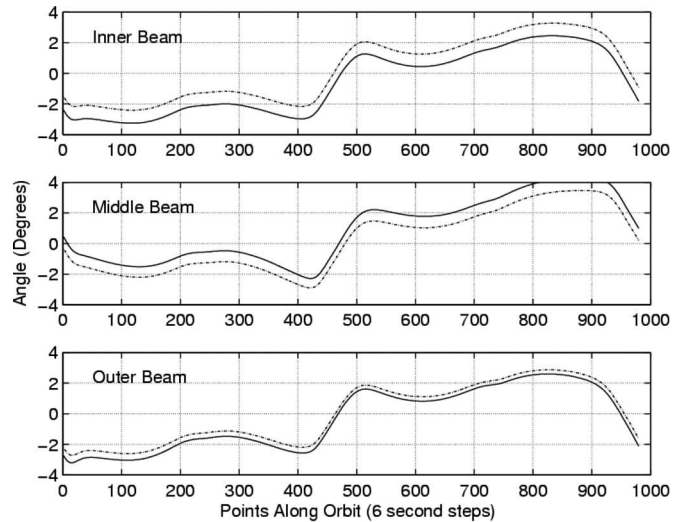


Fig. 8. Effect of Faraday rotation on the first Stokes parameter $I = T_v + T_h$ in the general case using the complete Aquarius antenna patterns. The top panel is for HSA, and the lower panel is for an ionosphere representative of LSA.

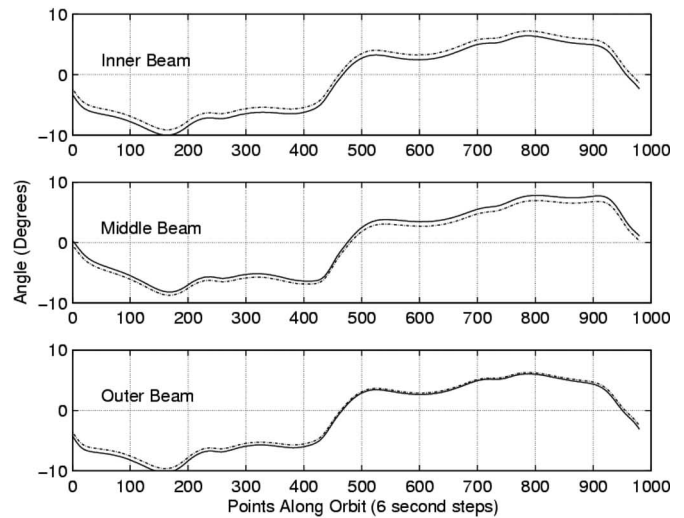
the dependence on Faraday rotation is more pronounced. The peak–peak change around the orbit is about 0.1 K in the case of LSA and about 0.2 K in the HSA case. This is still a small percentage change. The example suggests that the first Stokes parameter may be a good choice even when slight mismatches in the antenna pattern at each polarization are present. However, as noted previously, if an accuracy better than 0.1 K is required, then using first Stokes parameter to avoid Faraday rotation may not be sufficient. Fig. 8 suggests that, in this case, an additional correction for the rotation angle may be needed.

2) *Retrieved Rotation Angle*: Fig. 9 shows the angle that was retrieved using (12) for each beam, together with the Faraday rotation at boresight (dashed line). Fig. 9(a) presents the results in the case of LSA using the same ionosphere as in the previous examples. Fig. 9(b) is the same calculation but with an ionosphere corresponding to HSA. The general features are the same in the two cases, but the scale in Fig. 9(b) is different and corresponds to a much larger Faraday rotation.

Although the biases between the angle at boresight and the retrieved angle are different in the general case compared to either of the preceding special cases, they are still relatively constant over the orbit. In addition, they are about the same in both HSA and LSA. This is illustrated in Table III, which shows the mean value of the difference between the retrieved angle and the value at the beam boresight in the case of HSA and LSA. The column entitled “Mean Bias” is the average value of the difference between the solid and dashed curves in Fig. 9, and the column labeled “RMS Bias” is the rms value of this difference. The “RMS Bias” is also equivalent to the difference between the dashed curves in Fig. 9 and the solid line that is shifted by the mean value of the bias. This is an indication of how well one could correct for the bias if one had a reference point somewhere along the orbit to measure the offset. For example, if the satellite passed over a sounder where an accurate independent calculation of Faraday rotation could be made and used to remove the bias. Assuming such a procedure was used to correct the middle beam, Table III suggests that the error over the orbit would be on the order of 0.14° in the case of HSA.



(a)



(b)

Fig. 9. (a) Retrieved angle in the general case using the actual Aquarius antenna patterns. The dotted line is the value at the antenna boresight where there is no geometrical bias. This example is for a case of LSA. (b) Retrieved angle in the general case using the actual Aquarius antenna patterns. The dotted line is the value at the antenna boresight where there is no geometrical bias. This example is for a case of HSA. The results are similar to those shown in (a) (LSA), but the dynamic range is about 2.5 times larger.

TABLE III
BIAS IN THE GENERAL CASE

Beams	Mean Bias* (degrees)		RMS Bias (degrees)	
	LSA	HSA	LSA	HSA
Inner	0.827	0.833	0.024	0.050
Middle	-0.730	-0.688	0.057	0.138
Outer	0.341	0.401	0.067	0.170

* Mean difference between dashed and solid curve in Figure 9

V. DISCUSSION

In the analysis presented previously, it was shown that, when antenna pattern characteristics such as cross-polarization coupling are included, the first Stokes parameter $I = T_v + T_h$ is no longer completely independent of Faraday rotation and

also that the angle that was obtained from the second and third Stokes parameters, using (12), is biased relative to the Faraday rotation at boresight.

Assuming a well-designed antenna with small cross-polarization coupling, the dependence of I on Faraday rotation is of second order (less than 0.1% in Fig. 7). However, even at this level (0.12 K peak–peak), it can be important for the measurement of sea surface salinity where the sensitivity to changes in salinity is on the order of 0.5 K/psu. An uncertainty of 0.1 K is roughly 0.2 psu, which is the measurement goal of the Aquarius mission [4], [16].

Another approach to managing the effect of Faraday rotation is to try to measure the rotation angle. This can be done by measuring the third Stokes parameter and using (12) to retrieve the rotation angle. Two complicating factors are the presence of correlated fields at the surface [8] and departures of the antenna pattern from ideal. It was shown previously that, when taking into account realistic antenna patterns, a bias in the retrieved angle occurs. This is due in part to changes in geometry over the footprint of the main beam of the antenna (e.g., Fig. 3). Cross-polarization coupling also contributes a bias (e.g., Fig. 5). The biases depend on the antenna and its orientation, but the examples in Fig. 8 indicate that the biases are relatively stable over an orbit. Because of this, it may be possible to correct for the bias by comparing with an independent measurement of Faraday rotation. For example, if the sensor passes over a reference site (e.g., site of an ionospheric sounder) where the true Faraday rotation is known, it might be possible to use this value to correct for the bias. The column labeled “RMS Bias” in Table III is an indication of how well this might work. It suggests that correction to better than 0.17° might be possible.

Measuring the angle of Faraday rotation is equivalent to measuring the electron content of the ionosphere. For example, see (B3) in Appendix B. This could be of particular value over the ocean, where soundings to monitor the ionosphere are widely separated. Using the values in Table III as a measure of accuracy and the dynamic range in Fig. 9 as an indication of the magnitude of the change suggests that vertical total electron content (VTEC) could be measured with an accuracy of about 2%–3%. For a satellite in low earth orbit and HSA, this is on the order of 1 total electron content (TEC) unit (Fig. 1 in [1]).

APPENDIX A GENERAL CASE

The objective of this appendix is to provide explicit expressions for the integrand in (4)

$$T_A = \int G(\Omega)R(\Omega)T_B(\Omega)d\Omega \quad (A1)$$

where T_B is the brightness temperature at the surface, which is expressed in the form of the modified Stokes vector

$$T_B = \begin{bmatrix} T_v \\ T_h \\ T_3 \\ T_4 \end{bmatrix} \quad (A2)$$

where $T_3 = 2\alpha\text{Re}\langle E_h^*E_v \rangle$ and $T_4 = 2\alpha\text{Im}\langle E_h^*E_v \rangle$, and the coefficient of proportionality is $\alpha = \lambda^2/(\eta k)$, as defined in the text.

The matrix multiplications are done here in two steps. The first step is to evaluate the matrix product $T1 = R(\Omega)T_B(\Omega)$. The four rows of $T1$ are

$$\begin{aligned} T_{v1} &= \cos^2 \varphi_c T_v + \sin^2 \varphi_c T_h + 0.5 \sin 2\varphi_c T_3 \\ T_{h1} &= \sin^2 \varphi_c T_v + \cos^2 \varphi_c T_h - 0.5 \sin 2\varphi_c T_3 \\ T_{31} &= \sin 2\varphi_c T_v - \sin 2\varphi_c T_h - \cos 2\varphi_c T_3 \\ T_{41} &= -T_4. \end{aligned} \quad (A3)$$

The second step is to evaluate the matrix product $T2 = G(\Omega)T1(\Omega) = G(\Omega)[R(\Omega)T_B(\Omega)]$. The four rows of $T2$ are the elements of the integrand in (4). One obtains

$$\begin{aligned} T_{v2} &= |g_{vv}|^2(\cos^2 \varphi_c T_v + \sin^2 \varphi_c T_h + 0.5 \sin 2\varphi_c T_3) \\ &+ |g_{vh}|^2(\sin^2 \varphi_c T_v + \cos^2 \varphi_c T_h - 0.5 \sin 2\varphi_c T_3) \\ &+ \text{Re}(g_{vv}g_{vh}^*)(\sin 2\varphi_c T_v - \sin 2\varphi_c T_h - \cos 2\varphi_c T_3) \\ &+ \text{Im}(g_{vv}g_{vh}^*)T_4 \end{aligned} \quad (A4a)$$

$$\begin{aligned} T_{h2} &= |g_{hv}|^2(\cos^2 \varphi_c T_v + \sin^2 \varphi_c T_h + 0.5 \sin 2\varphi_c T_3) \\ &+ |g_{hh}|^2(\sin^2 \varphi_c T_v + \cos^2 \varphi_c T_h - 0.5 \sin 2\varphi_c T_3) \\ &+ \text{Re}(g_{hv}g_{hh}^*)(\sin 2\varphi_c T_v - \sin 2\varphi_c T_h - \cos 2\varphi_c T_3) \\ &+ \text{Im}(g_{hv}g_{hh}^*)T_4 \end{aligned} \quad (A4b)$$

$$\begin{aligned} T_{32} &= 2\text{Re}(g_{vv}g_{hv}^*)(\cos^2 \varphi_c T_v + \sin^2 \varphi_c T_h + 0.5 \sin 2\varphi_c T_3) \\ &+ 2\text{Re}(g_{hh}^*g_{vh}) \\ &\times (\sin^2 \varphi_c T_v + \cos^2 \varphi_c T_h - 0.5 \sin 2\varphi_c T_3) \\ &+ \text{Re}(g_{vv}g_{hh}^* + g_{vh}g_{hv}^*) \\ &\times (\sin 2\varphi_c T_v - \sin 2\varphi_c T_h - \cos 2\varphi_c T_3) \\ &+ \text{Im}(g_{vv}g_{hh}^* - g_{vh}g_{hv}^*)T_4 \end{aligned} \quad (A4c)$$

$$\begin{aligned} T_{42} &= 2\text{Im}(g_{vv}g_{hv}^*)(\cos^2 \varphi_c T_v + \sin^2 \varphi_c T_h + 0.5 \sin 2\varphi_c T_3) \\ &+ 2\text{Im}(g_{hh}^*g_{vh}) \\ &\times (\sin^2 \varphi_c T_v + \cos^2 \varphi_c T_h - 0.5 \sin 2\varphi_c T_3) \\ &+ \text{Im}(g_{vv}g_{hh}^* + g_{vh}g_{hv}^*) \\ &\times (\sin 2\varphi_c T_v - \sin 2\varphi_c T_h - \cos 2\varphi_c T_3) \\ &- \text{Re}(g_{vv}g_{hh}^* - g_{vh}g_{hv}^*)T_4. \end{aligned} \quad (A4d)$$

In computing the general cases that are illustrated in Figs. 8 and 9, the expressions given in (A4a)–(A4d) were used in the special case $T_3 = T_4 = 0$. That is, it is assumed that the third and fourth Stokes parameters at the surface are zero.

APPENDIX B ROTATION ANGLES

I. Faraday Rotation

The rotation of the polarization vector of a linearly polarized plane wave propagating along path S from $[0, L]$ is [20], [21]

$$\Phi_F = (\pi/c\nu^2) \int_0^L \nu_p^2(s) \nu_B(s) \cos(\Theta_B(s)) ds \quad (\text{B1})$$

where ν is the frequency; ν_p and ν_B are the plasma and gyro frequencies, respectively; and Θ_B is the angle between the propagation vector and magnetic field, which is given by

$$\Theta_B = \cos(\theta) \sin(I) - \sin(\theta) \cos(I) \cos(\varphi - D). \quad (\text{B2})$$

In the preceding expression, (θ, φ) are the polar coordinates of the line of sight from the spacecraft to the observation point on the surface, and (I, D) are the local magnetic “dip” angle and declination, respectively.

At L-band (1.4 GHz), (B1) can be simplified, and to a reasonable approximation, one obtains [21]

$$\Phi_F \approx 6950 B_{400} \cos(\Theta_B) \sec(\theta_P) \text{VTEC} \quad (\text{B3})$$

where θ_P is the angle between the propagation vector and nadir, B_{400} is the value of the magnetic field at 400 km, and VTEC is the vertical total electron content.

In the calculations that were presented in this paper, the Faraday rotation angle Φ_F has been obtained by applying (B3) using parameters above the midpoint of the propagation path between the surface and the spacecraft. B_{400} and Θ_B are evaluated using the magnetic field at 400 km above this point, and VTEC is the electron content in the vertical column above this point up to the altitude of the spacecraft. The TEC is computed using the IRI-2000 to model the ionosphere [18], and the magnetic field is obtained from the IGRF [19]. In the examples that were presented here, the ionosphere for November 14, 2004 was used for LSA, and that for November 14, 2001 was used for HSA.

II. Geometrical Rotation

The angle $\varphi_c = \varphi + \Phi_F$ that is needed in the rotation matrix (6) consists of the Faraday rotation Φ_F , which was described previously, and the angle φ , due to the fact that the polarization vectors (\mathbf{h}, \mathbf{v}) at an arbitrary point on the surface are not aligned with the definitions at the antenna.

For the antenna, the “Ludwig-3” definition (3) is used to define polarization [11]. It is assumed that, at the antenna boresight, the “vertical” polarization port of the antenna is aligned with the conventional radiometric definition of vertical polarization at the surface. In the local antenna coordinate system $(\mathbf{x}, \mathbf{y}, \mathbf{z})$, this direction is assigned to the x -axis, and the z -axis is along the boresight. With this definition, vertical polarization at boresight is aligned with $\boldsymbol{\varepsilon}_1$, as defined in (3). Unfortunately, the Ludwig-3 definition uses the “radar” definition of polarization (i.e., looking away from the antenna),

and in radiometry, it is conventional to define \mathbf{v} and \mathbf{h} as if propagating away from the surface toward the antenna. The result is that, at boresight, the direction of horizontal polarization in the antenna reference frame $\boldsymbol{\varepsilon}_2$ is now opposite to the direction of \mathbf{h} at the surface ($\mathbf{h} \bullet \boldsymbol{\varepsilon}_2 = -1$ at boresight). This sign difference becomes an annoyance that must be kept in mind when dealing with antenna patterns, which are usually delivered in conventional coordinates.

At points other than boresight, the antenna polarization is given by $\boldsymbol{\varepsilon}_1$ and $\boldsymbol{\varepsilon}_2$, as defined in (3). These vectors are orthogonal and orthogonal to the line-of-sight between the antenna and surface, but they are rotated with respect to the corresponding values at the surface, i.e.,

$$\begin{aligned} \mathbf{v} \bullet \boldsymbol{\varepsilon}_1 &= \cos(\varphi) \\ \mathbf{h} \bullet \boldsymbol{\varepsilon}_1 &= -\sin(\varphi). \end{aligned} \quad (\text{B4})$$

In (B4), φ is the angle by the same name in (3) and is the “azimuth” in a conventional spherical coordinate system that is centered on the local antenna coordinates $(\mathbf{x}, \mathbf{y}, \mathbf{z})$. It is measured from the x -axis and is positive in the direction toward the positive y -axis in the antenna coordinate system.

REFERENCES

- [1] D. M. Le Vine and S. Abraham, “Faraday rotation and passive microwave remote sensing of soil moisture from space,” in *Microwave Radiometry & Remote Sensing of the Earth’s Surface and Atmosphere*, P. Pampaloni and S. Paloscia, Eds. Zeist, The Netherlands: VSP, 2000, pp. 89–96.
- [2] Y. H. Kerr, P. Waldteufel, J. P. Wigneron, J. M. Martinuzzi, B. Lazard, J. M. Goutoule, and A. Lannes, “The Soil Moisture and Ocean Salinity mission: An overview,” in *Microwave Radiometry & Remote Sensing of the Earth’s Surface and Atmosphere*, P. Pampaloni and S. Paloscia, Eds. Zeist, The Netherlands: VSP, 2000, pp. 467–475.
- [3] Y. Kerr *et al.*, “Soil moisture retrieval from space: The Soil Moisture and Ocean Salinity (SMOS) mission,” *IEEE Trans. Geosci. Remote Sens.*, vol. 39, no. 8, pp. 1729–1735, Aug. 2001.
- [4] D. Le Vine, G. Lagerloef, F. Pellerano, S. Yueh, and R. Colomb, “Aquarius: A mission to monitor sea surface salinity from space,” in *Proc. MicroRad*, San Juan, Puerto Rico, 2006, pp. 87–90.
- [5] D. M. Le Vine, G. S. E. Lagerloef, R. Colomb, S. Yueh, and F. Pellerano, “Aquarius: An instrument to monitor sea surface salinity from space,” *IEEE Trans. Geosci. Remote Sens.*, vol. 45, no. 7, pp. 2040–2050, Jul. 2007.
- [6] S. Abraham and D. M. Le Vine, “Evaluation of IRI-95 to correct errors caused by Faraday rotation in passive microwave remote sensing from space,” *Adv. Space Res.*, vol. 27, no. 1, pp. 153–156, 2001.
- [7] G. S. E. Lagerloef, C. Swift, and D. M. Le Vine, “Sea surface salinity: The next remote sensing challenge,” *Oceanography*, vol. 8, no. 2, pp. 44–50, 1995.
- [8] S. Yueh, “Estimates of Faraday rotation with passive microwave polarimetry for microwave remote sensing of earth surfaces,” *IEEE Trans. Geosci. Remote Sens.*, vol. 38, no. 5, pp. 2434–2438, Sep. 2000.
- [9] S. Ribó and M. Martín-Neira, “Faraday rotation correction in the polarimetric mode of MIRAS,” *IEEE Trans. Geosci. Remote Sens.*, vol. 42, no. 7, pp. 1405–1410, Jul. 2004.
- [10] T. Meissner and F. J. Wentz, “Polarization rotation and the third Stokes parameter: The effects of spacecraft attitude and Faraday rotation,” *IEEE Trans. Geosci. Remote Sens.*, vol. 44, no. 3, pp. 506–515, Mar. 2006.
- [11] A. Ludwig, “The definition of cross polarization,” *IEEE Trans. Antennas Propag.*, vol. AP-21, no. 1, pp. 116–119, Jan. 1973.
- [12] A. Camps, I. Corbella, F. Torres, M. Vall-Ilossera, and N. Duffo, “Polarimetric formulation of the visibility function equation including cross-polar antenna patterns,” *IEEE Geosci. Remote Sens. Lett.*, vol. 2, no. 3, pp. 292–295, Jul. 2005.
- [13] A. K. Fung, *Microwave Scattering and Emission Models and Their Applications*. Norwood, MA: Artec House, 1994.
- [14] L. Tsang, J. A. Kong, and R. T. Shin, *Theory of Microwave Remote Sensing*. Hoboken, NJ: Wiley, 1985.

- [15] E. Dinnat and D. M. Le Vine, "Effects of the antenna aperture on remote sensing of sea surface salinity at L-band," *IEEE Trans. Geosci. Remote Sens.*, vol. 45, no. 7, pp. 2051–2060, Jul. 2007.
- [16] A. Sen, Y. Kim, D. Caruso, G. Lagerloef, R. Colomb, D. Le Vine, and S. Yueh, "Aquarius/SAC-D mission overview," in *Proc. SPIE Conf.—Sensors, Systems, and Next-Generation Satellites X*, Stockholm, Sweden, Sep. 2006, vol. 6361, p. 63610I. DOI: 10.1117/12.691981.
- [17] J. Vacchione, unpublished communication.
- [18] D. Bilitza, "International reference ionosphere 2000," *Radio Sci.*, vol. 36, no. 2, pp. 261–265, 2001.
- [19] E. Barton, "International geomagnetic reference field: The seventh generation," *J. Geomagn. Geoelectr.*, vol. 49, no. 2/3, pp. 123–148, 1997.
- [20] A. R. Thompson, J. M. Moran, and G. W. Swenson, *Interferometry and Synthesis in Radio Astronomy*. New York: Wiley, 1986.
- [21] D. M. Le Vine and S. Abraham, "The effect of the ionosphere on remote sensing of sea surface salinity from space: Absorption and emission at L band," *IEEE Trans. Geosci. Remote Sens.*, vol. 40, no. 4, pp. 771–782, Apr. 2002.



David M. Le Vine (M'70–SM'79–F'95) received the B.S. and M.S. degrees in electrical engineering, the M.S. degree in physics, and the Ph.D. degree in electrical engineering from the University of Michigan, Ann Arbor.

He is currently with the Instrument Sciences Branch, Laboratory for Hydrospheric and Biospheric Sciences, Goddard Space Flight Center, Greenbelt, MD, where he does research to develop techniques for microwave remote sensing of the environment from space. His research has focused on passive remote sensing at the long wavelength end of the microwave spectrum (e.g., L-band) with applications to remote sensing of soil moisture and sea surface salinity. An example of this work is the development of the synthetic aperture radiometer ESTAR and its successor 2D-STAR. He is currently the Deputy Principle Investigator for Aquarius, which is a NASA Earth System Science Pathfinder mission to measure sea surface salinity. He is also a member of the Science Advisory Group for the European Space Agency's Soil Moisture and Ocean Salinity (SMOS) mission. His experience includes the Department of Electrical Engineering, University of Maryland at College Park, MD, and adjunct faculty at the George Washington University, Washington, DC.

Dr. Le Vine is a member of the Geoscience and Remote Sensing Society (GRSS), Antennas and Propagation Society, GRSS AdCom, International Union of Radio Science (URSI), and the American Geophysical Union.



S. Daniel Jacob received the B.E. degree (Hons.) in civil engineering from Madurai Kamaraj University, Madurai, India, the M.S. degree in ocean engineering from the Indian Institute of Technology, Madras, and the Ph.D. degree in meteorology and physical oceanography from the University of Miami, Miami, FL, in 2000.

He was a Research Scientist at the Indian Space Research Organization, where he analyzed synthetic aperture radar data of ocean surface waves and other satellite data before working toward the Ph.D. degree. He served as a Postdoctoral Research Associate at the University of Miami, where he was involved in acquiring oceanographic data from the NOAA hurricane hunters using expendable probes and in the Eastern Pacific as part of the Eastern Pacific Investigation of Climate project. As a member of the Aquarius science simulator team in the Goddard Earth Science and Technology Center, Goddard Space Flight Center, Greenbelt, MD, he is involved in the development of the forward model and also conducts research on the effects of surface forcing and ocean mixing on sea surface salinity.



Emmanuel P. Dinnat was born in Sarcelles, France, in 1975. He received the DEA degree in instrumental methods in astrophysics and their spatial applications and the Ph.D. degree in computer science, telecommunications, and electronics from the University of Paris VI, Paris, France, in 1999 and 2003, respectively.

He is currently with the Goddard Earth Science and Technology Center, Goddard Space Flight Center (GSFC), Greenbelt, MD. From 1999 to 2003, he was with the Laboratoire d'Océanographie Dynamique et de Climatologie (LODYC), Paris, where he pursued the Ph.D. degree on the subject of remote sensing of sea surface salinity by means of passive microwave measurements at L-band, in the frame of the European Space Agency (ESA) mission: Soil Moisture and Ocean Salinity (SMOS). His focus was on the modeling of the sea surface emissivity and the inversion of salinity from radiometric measurements. From 2003 to 2005, he was with the ESA European Space Research and Technical Centre (ESTEC), Noordwijk, The Netherlands, where he studied the concept of using active instruments for correcting for the roughness effects in the scope of salinity retrieval using radiometers. In 2005, he joined NASA GSFC to work on the NASA/CONAE salinity mission Aquarius/SACD. His research interests are active and passive microwave remote sensing, sea surface salinity, scattering from rough surfaces, atmospheric radiative transfer, and numerical simulation of radiative transfer.

Dr. Dinnat is a member of the American Geophysical Union. In 2006, he was the recipient of the peer award for outstanding PostDoc/Research Associate from the GSFC's Hydrospheric and Biospheric Sciences Laboratory.



Paolo de Matthaeis (M'95) was born in Rome, Italy. He received the Laurea degree (*summa cum laude*) in electrical engineering from the University of Rome "Tor Vergata," Rome, in 1991 and the Doctor of Science degree in electrical engineering from George Washington University, Washington, DC, in 2005.

From 1993 to 1994, he was with the European Space Research and Technical Centre (ESTEC), ESA, Noordwijk, The Netherlands, under the Young Graduate Trainee program. From 1994 to 1995, he received a grant from the Italian Space Agency (ASI)

to carry out research in the SIR-C/X-SAR data at the Remote Sensing Laboratory, University of Rome "Tor Vergata." He is currently with the Goddard Earth Science and Technology Center, Goddard Space Flight Center, Greenbelt, MD. His research work includes active and passive microwave remote sensing, with special interest in electromagnetic modeling of vegetation and sea surface. He is part of the Science Algorithms team for the Aquarius instrument.



Saji Abraham (M'01–SM'03) received the B.Sc. degree in physics from Kerala University, Trivandrum, India, the M.Sc. degree in space physics from Andhra University, Visakhapatnam, India, and the Ph.D. degree in space physics from the University of Delhi, Delhi, India. He is currently working toward the M.S. degree in the Department of Electrical and Computer Engineering, Johns Hopkins University, Baltimore, MD.

He has been supporting NASA projects since 1997. He is currently with RS Information Systems, Inc., Goddard Space Flight Center, Greenbelt, MD. He had been working on wide areas of ionosphere radio wave propagation techniques and published scientific articles on lower ionosphere dynamics and its coupling with the lower atmosphere through planetary waves and quasi-biennial oscillations. His research interests are developing forward models to simulate brightness temperature at microwaves for spaceborne sensors and sea surface salinity retrieval algorithms.

Dr. Abraham is a member of the American Geophysical Union.